

1 *Type of the Paper (Article, Review, Communication, etc.)*

2 **Travelling Surface Plasmons with Interference**

3 **Envelope and A Vision for Time Crystals**

4 **Amir Djalalian-Assl**^{1,*}

5 * Correspondence: amir.djalalian@gmail.com

6 **Abstract:** The influence of the film thickness and the substrate's refractive index on the surface
 7 mode at the superstrate is an important study step that may help clearing some of the
 8 misunderstandings surrounding their propagation mechanism. A single sub-wavelength slit
 9 perforating a thin metallic film is among the simplest nanostructure capable of launching Surface
 10 Plasmon Polaritons on its surrounding surface when excited by an incident field. Here, the impact
 11 of the substrate and the film thickness on surface waves is investigated. When the thickness of the
 12 film is comparable to its skin depth, SPP waves from the substrate penetrate the film and emerge
 13 from the superstrate, creating a superposition of two SPP waves, that leads to a beat interference
 14 envelope with well-defined loci which are the function of both the drive frequency and the
 15 dielectric constant of the substrate/superstrate. As the film thickness is reduced to the SPP's
 16 penetration depth, surface waves from optically denser dielectric/metal interface would dominate,
 17 leading to volume plasmons that propagate inside the film at optical frequencies. Interference of
 18 periodic volume charge density with the incident field over the film creates charge bundles that are
 19 periodic in space and time.

20 **Keywords:** SPP; Time Crystal, Thin Film

22 **1. Introduction**

23 In a most relevant report (to a certain extent) Wang *et. al.*[1] modelled a free standing optically
 24 thin silver film in vacuum, where authors try to explain their findings in terms of long range SPPs,
 25 SPP Wave Packets and Quasi Cylindrical Waves (QCW) ... etc. Prior to that, Verhagen *et. al.* showed
 26 that guided waves in a metal-dielectric-metal waveguide can penetrate the thin metallic cladding
 27 hence shortening the wavelength of the SPPs at the silver/air interface [2].

28 When the refractive index of the substrate differs from that of the superstrate, however, the
 29 superposition of the two waves from both sides of the film leads to travelling SPP waves modulated
 30 by a well define non-travelling interference envelope at metal/dielectric interfaces. For a sufficiently
 31 thin metallic layer, SPPs formed at the metal/superstrate also interfere with those formed at the
 32 metal/substrate within the metal leading to a non-travelling periodic electric polarization inside the
 33 film. Note that this report is not concerned with the SPP eigenmodes [3-5], but rather it is an
 34 investigation on surface wave interference under the forced vibration. The numerical results
 35 reported here are exactly those included in chapter 10 of my thesis [6]. However, during the internal
 36 review, pre- and post-examination period of my thesis, it was requested that I remove the notions of
 37 Lorentz force and periodic transparency. This version of the report has those notions restored and
 38 used for explaining the mechanism behind the plasmonic time-crystal and more.

39 Let's start with the fundamental equations governing the surface plasmons polaritons (SPP)
 40 stated here for convenience [7]:

$$41 \quad k_{SPP} = \sqrt{\frac{\epsilon_m \epsilon_d}{\epsilon_m + \epsilon_d}} k \equiv k'_{SPP} + i k''_{SPP} \quad (1)$$

$$42 \quad k_m \approx \sqrt{\frac{\epsilon_m^2}{\epsilon_m + \epsilon_d}} k \equiv k'_m + i k''_m \quad (2)$$

43 There is also a very useful presentation by Rosa [8] that would also help the reader to gain
 44 background knowledge on SPPs. Not having access to the university resource, I could not cite the
 45 references in that presentation. So I hope citing Rosa's work would suffice for now.

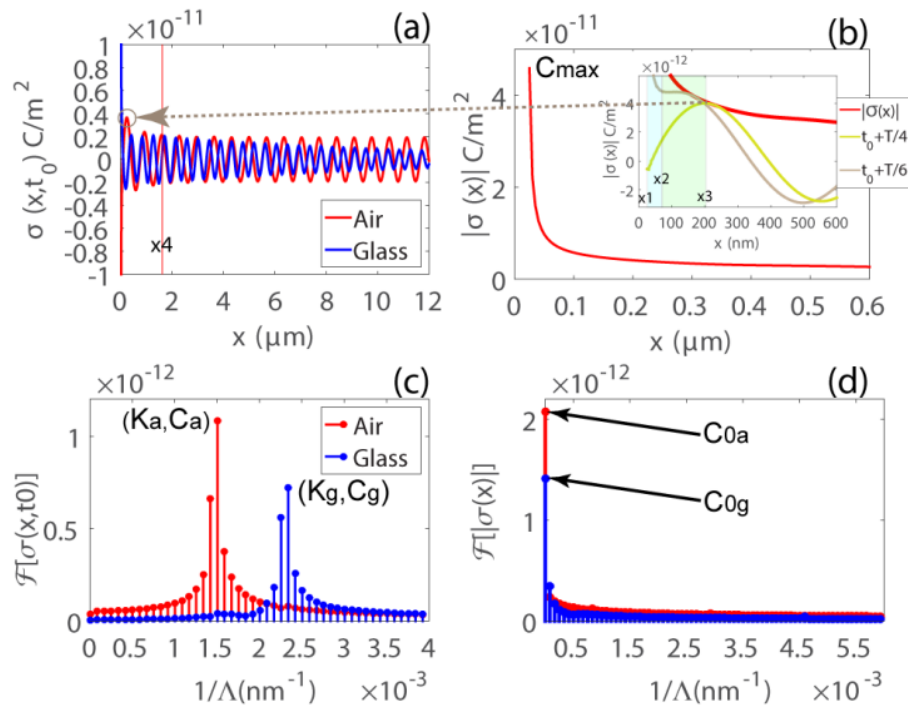
46 Consider a metallic thin film with its surface set parallel to the x - y plane, equation (1) describes
 47 the complex wave vector for the SPP waves propagating at the metal/dielectric interface along the
 48 x - y plane, whereas the wave vector for the SPP waves penetrating the metallic film in the z -direction
 49 is given by equation (2). In both equations the real part of the wave vector represents propagation
 50 constant, whereas the imaginary part defines the decay lengths, $1/k_{SPP}''$ and $1/k_m''$, over which the
 51 SPP's amplitude decreases by $1/e$. Note that in equation (2), the permittivity, ϵ_d , corresponds to the
 52 dielectric material from which the field penetrates the film.

53 The short introduction above was aimed to highlight some of the key features of surface
 54 plasmon polaritons relevant to this report. What will follow is a theoretical study on SPPs launched
 55 by a single subwavelength aperture perforated in a silver thin film. Section 2.1 covers the influence
 56 of the film thickness and the refractive index of the supporting substrate on the SPPs and in section
 57 2.2 a plasmonic time crystal is proposed.

58 2. Results and Discussions

59 2.1 The Origin of Modulating Envelope in SPPs over Flat Metallic Films

60 A 2D Finite Element Method (FEM) model of a 100 nm thick silver film perforated with a 50 nm
 61 wide slit was simulated. Modelling time harmonics with FEM is particularly useful in examining the
 62 steady-state response of the system under the continuous excitation with an incident wave with a
 63 single wavelength. The refractive index of the glass substrate supporting the film was initially set to
 64 $n_1 = 1.52$ and the refractive index data for silver was taken from Palik [9]. The film was along the x
 65 plane and was illuminated with a normally incident TM wave propagating in the $+z$ -direction from
 66 glass substrate. For convenience the air/silver interface is denoted by $z = z_0$. Figure 1(a) depicts the
 67 distribution of the real part of surface charge densities, $\sigma(x, t) = |\sigma(x)| e^{i(k_{SPP}x - \omega_0 t)}$, at an arbitrary time
 68 t_0 , calculated at both the air/silver and glass/silver interfaces from the normal to the surface, i.e. the
 69 z -component of the electric field. The amplitude, i.e. the envelope, of the surface charge density at
 70 the air/silver interface was calculated using $|\sigma(x)| = \sqrt{\sigma(x, t)\sigma(x, t)^*}$ and is depicted in Figure 1(b).
 71 The corresponding Fast Fourier Transforms (FFT), $f[\sigma(x, t_0)]$ and $f[|\sigma(x)|]$ were also
 72 calculated, see Figure 1(c)-(d).
 73



74

75 Figure 1: (a) Surface charge density, $\sigma(x, t_0)$, at an arbitrary time t_0 , calculated at the air/silver and
 76 glass/silver interfaces. (b) The envelope, $|\sigma(x)|$, at the air/silver interface. The corresponding FFT of
 77 (c) the wave $f[\sigma(x, t_0)]$ and (d) the envelope $f[|\sigma(x)|]$.

78

79 In Figure 1(b), the maximum accumulated charge density at the edge of the cavity, $x_1 = 25$ nm, is
 80 labelled C_{max} . The decay length of the surface charge density, where the value of the C_{max} drop by $1/e$,
 81 was found to be ~ 10 nm from the edge (or 35 nm from the center). At $\lambda_0 = 700$ nm, the decay length of
 82 an SPP along the silver/air interface is ~ 67 μm [7]. Activities near the slit, therefore, may not be
 83 considered as SPPs as they are highly localized. The inset of Figure 1(b), depict the $|\sigma(x)|$ and $\sigma(x, t)$
 84 at $t = t_0 + T/6$ and $t_0 + T/4$. Here, T is the period and t_0 was set to a time when the surface charge
 85 density was at its maximum, C_{max} , at x_1 . The separation between the localized surface charges and
 86 the appearance of the harmonic wave occurs at $t = t_0 + T/6$ and $x_2 \approx 75$ nm, i.e. 50 nm away from the
 87 edge. In fact, the 10 nm decay length, closer to the $1/k_m'' \approx 25$ nm obtained from equation (2),
 88 indicates that the surface charges in the vicinity of the slit are due to the cavity modes, penetrating
 89 the metal and subsequently decaying rapidly. This agrees to previous works [10,11]. Furthermore, at
 90 $t = t_0 + T/4$ the surface charge density at x_1 drops to 0 and the peak at $x_3 = 200$ nm resembles that of a
 91 harmonic wave. The phase difference of 90° between the oscillations at x_1 and x_3 , resembles that of a
 92 forced vibration where the force leads the displacement by 90° under resonance conditions [12].
 93 However, the amplitude of the first peak at x_3 is $1.9 \times C_{0a}$, where C_{0a} is the DC component of $|\sigma(x)|$,
 94 hence the average amplitude of the travelling SPP waves, see Figure 1(a) and (d). Note FFT of the
 95 envelope, $f[|\sigma(x)|]$, in Figure 1(d), identifies the DC components (or the amplitudes of the SPP
 96 waves), C_{0a} and C_{0g} at both interfaces.

97 By examining Figure 1(a) it was determined that the amplitude of the wave drops to C_{0a} at $x_4 \approx$
 98 $w/2 + 2 \times \lambda_{SPP}$, i.e. 2 wavelengths away from the edge of the slit. Although the surface charge density
 99 resembles that of a harmonic oscillation in the $x_3 \leq x \leq x_4$ range, its rapid decay and non-conformance
 100 to the $1/k_{SPP}''$, suggests a kind of transient state. To evaluate the λ_{SPP} , FFT transform $f[\sigma(x, t_0)]$ was
 101 calculated for both the silver/air and the silver/glass interfaces, Figure 1(c). The weighted
 102 average, $K_{SPP} = \sum_{i=1}^5 (K_{SPPi} C_{SPPi}) / C_{SPPi}$, that included the center mode and the four immediate

103 neighboring modes, i.e. two on each side of the maxima, provides a good estimate of SPP
 104 wavenumbers. The SPP wavelengths were then calculated using $\lambda_{\text{SPP}} = 1/K_{\text{SPP}}$, where
 105 $K_{\text{SPP}} = \text{Re}(k_{\text{SPP}})/2\pi$ is the wavenumber obtained from FFT.

106 For the sake of brevity in notations, let the subscripts “a” and “g” be denoting the association of
 107 physical quantities carried by the SPP waves at the superstrate (air) and substrate (glass and later
 108 diamond) respectively. So, in summary, $\lambda_a = 1/K_a = 667$ nm and $\lambda_g = 1/K_g = 427$ nm are in agreement
 109 with $\lambda_a = 682$ nm and $\lambda_g = 433$ nm obtained analytically using equation (1). Examining the $|\sigma(x)|$, an
 110 additional spatial second harmonic were observed in the envelope at both interfaces. The second
 111 harmonics in the envelope seems to be the result of superposition of two time-harmonic waves:

$$112 \quad \sigma(x, t) = E_z e^{i(k_a x - \omega t)} + E_z' e^{i(-k_a x - \omega t + m\pi)} \quad (3)$$

113 where m must be an even integer and $E_z \gg E_z'$. However, the origin of the second term in
 114 equation (3), E_z' , is unknown. The boundary conditions were set to eliminate all reflections,
 115 therefore, simulation artefacts cannot account for such periodic perturbations, even more so that
 116 such second harmonics do not manifest themselves over the surface of a Perfect Electric Conductor
 117 (PEC) that does not support SPPs!

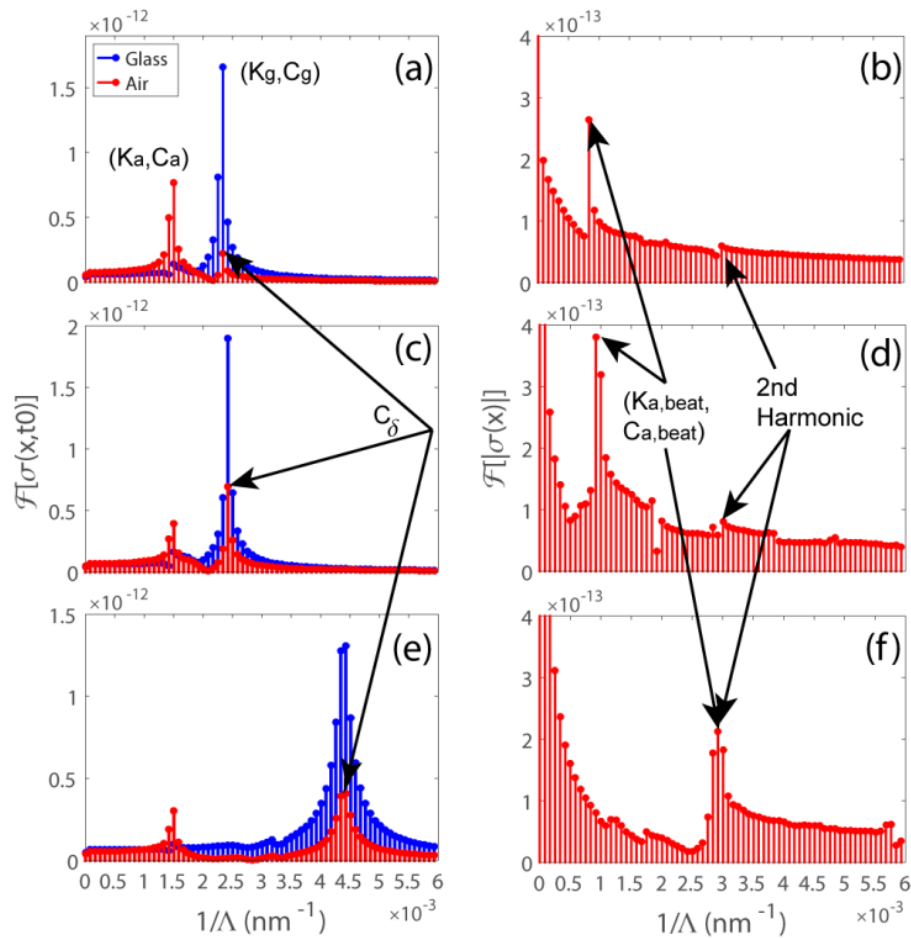
118 A possible scenario that may lead to oscillations at double the fundamental frequency in $|\sigma(x)|$,
 119 is the normal-to-the-surface component of SPPs being modulated by the parallel-to-the-surface
 120 component at the interface via a relationship that involved multiplication. SPPs are longitudinal
 121 waves manifested as surface charge bundles, where charges in each bundle are held together by
 122 SPP's E_z along the x -axis. Repelling/attracting Coulomb forces from each bundle to its neighboring
 123 charge bundles of equal/opposite signs, is analogous to a chain of masses attached to one another by
 124 springs. Given that the oscillation along the chain is being driven by $F \propto \sigma(x, t) E_x(z_0, t)$ from the
 125 aperture, it is plausible to attribute the origin of the backward propagating term in equation (3) to
 126 $F_x \propto e^{-i2(k_a x - \omega t)}$, where the push/pull by F_x generates the backward propagating waves. Basically, the
 127 force modulates the amplitude of the surface charge density wave over $T/2$, during which the SPP
 128 has travelled a total distance of $\lambda_g/2$. Having noted that, the exact form of a partial differential
 129 equation governing the forced vibration that leads to equation (3) as a solution is yet to be
 130 determined.

131 Regardless, it was envisaged that by reducing the film thickness, it would be possible for
 132 surface charge densities from the glass/silver interface manifest themselves at the air/silver interface,
 133 leading to a superposition of the two waves:

$$134 \quad \sigma(x) = \left[2e^{i\left(\frac{k_a + k_g}{2}\right)x} \cos\left(\frac{(k_a - k_g)x}{2}\right) \right] \quad (4)$$

135 see Appendix A. This would modulate the charge densities along the x -direction, resulting in a
 136 series of minima/maxima with fixed loci that are $1/K_{\text{beat}}$ apart, where $K_{\text{beat}} \equiv |K_a - K_g|$. Hence by
 137 controlling the film thickness and the refractive index of the substrate, one could control the
 138 modulation strength and frequency of the envelope. Keeping the superstrate and the substrate intact
 139 as before, two additional simulations, with $h = \{50, 25\}$ nm, were carried out in order to investigate
 140 the influence of the film thickness. Figure 2 depict the numerically calculated $f[\sigma(x, t_0)]$ and
 141 $f[|\sigma(x)|]$. Figure 2(a), (c) and (e) depicts $f[\sigma(x, t_0)]$ with $h = \{50, 25\}$ nm when the film is supported
 142 on a glass substrate and with $h = 25$ nm on a diamond substrate respectively. In all cases, K_a was
 143 found to be at the same position as it was for $h = 100$ nm. For $h = \{50, 25\}$ nm on a glass substrate, K_g
 144 was also found to be at the exact location as it was for the 100 nm thick silver film. In the case of the
 145 diamond substrate, $\lambda_g = 1/K_g = 230$ nm, was found to be close to the $\lambda_g = 246$ nm calculated using
 146 equation (1). In all cases, the appearance of an additional peak at the air/silver interface, positioned
 147 at K_g having an amplitude $C_{\delta_g} = C_g e^{-\frac{z}{\delta}}$, corresponded to the SPP waves that travel along the
 148 substrate/silver interface penetrating the film and emerging at the air/silver interface. Presence of

149 SPPs with wavelength λ_g at air/silver interface is significant as it impacts the design criteria for
 150 plasmonic meta-surfaces. FFT of the corresponding envelopes, $f[|\sigma(x)|]$, in Figure 2(b), (d) and (f),
 151 show the anticipated modulating envelope with $K_{\text{beat}} \equiv |K_a - K_g|$.
 152

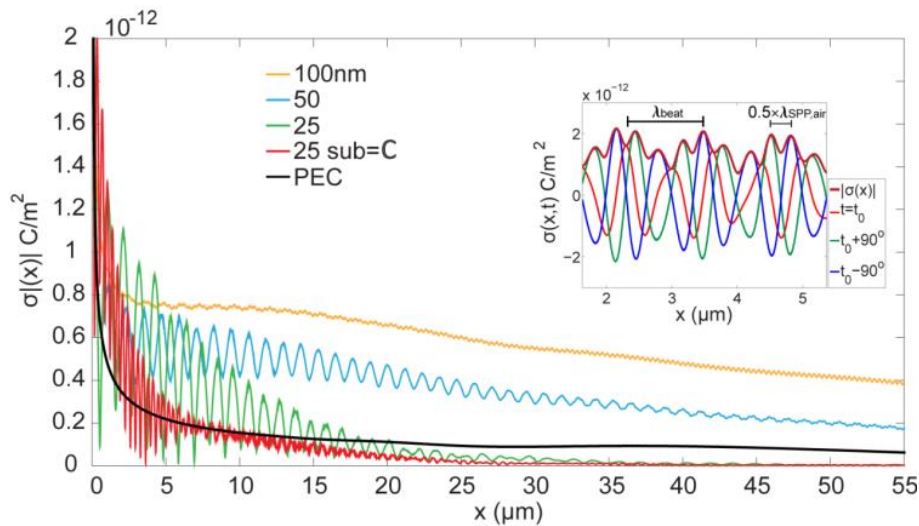


153

154 Figure 2: $f[|\sigma(x,t_0)|]$ and $f[|\sigma(x)|]$ calculated for (a)-(b) $h = 50$ nm on glass substrate, (c)-(d) $h =$
 155 25 nm on glass substrate and (e)-(f) $h = 25$ nm on diamond substrate. Note that subscript 'g' is used to
 156 label the substrate in general.

157 Note that in order to shift the K_{beat} to overlap with the second harmonics observed in the
 158 envelope, the required value for the substrate's refractive index was found to be (see Appendix A)
 159 $n_1 = 2.41$ at $\lambda_0 = 700$ nm that corresponds to diamond [13]. With the recent advances in
 160 nano-diamond technology, use of diamond substrate is both feasible and practical [14]. Therefore, an
 161 additional simulation was carried out with a 25 nm thick silver film supported on a diamond
 162 substrate.

163 Figure 3 depicts the modulating envelopes, $|\sigma(x)|$, calculated over the air/silver interface for
 164 $h = \{100, 50, 25\}$ nm when the film is supported on a glass substrate and for $h = 25$ nm with a diamond
 165 substrate. The aperture was normally illuminated with a Gaussian beam, $15 \times \lambda_0$ in waist, from the
 166 substrate. The surface of a perfect electric conductor (PEC) that neither supports SPPs nor allows the
 167 penetration of the fields, produced only a smooth line, see Figure 3-(line in black). Values for the
 168 PEC line were calculated using $\epsilon_0 E_z$ to retain the C/m² unit. The inset in Figure 3 shows the
 169 travelling SPPs, $\sigma(x, t)$, that are modulated by the envelope $|\sigma(x)|$, calculated over the air/silver
 170 interface for the case $h = 50$ nm when excited with a plane wave from the glass substrate. The
 171 presence of the second harmonic and the beat interference in the envelope are marked.



172

173

174

Figure 3: Surface charge densities, $|\sigma(x)|$, over the air/silver surface for $h = \{100, 50, 25\}$ on glass substrate, $h = 25$ nm on diamond substrate and for PEC.

175

176

177

178

179

180

181

182

183

184

185

186

187

188

189

190

191

A noticeable feature in Figure 3 is the relation between the SPP's decay length, $1/k_{SPP}''$, along the air/silver interface and the strength (or the amplitude) of the interference envelope. Travelling SPP waves along the air/silver interface may be described as the superposition of two waves according to equation (17) in Appendix A, where each component decay according to their respective decay length $1/k_a''$ and $1/k_g''$. Analytical values for decay lengths were found to be $\{67, 17, 3.2\}$ μm for the air/silver, glass/silver and diamond/silver interfaces respectively. This explains the decay length of the envelope clearly. For example, in the case of the 25 nm silver film supported on a diamond substrate, the amplitude of the $C_{\delta_g} e^{i(k_g x - \omega t)}$ component drops to $1/e$ of its maximum at $x = 3.2$ μm , beyond which the only component that continues to propagate is $C_{0a} e^{i(k_a x - \omega t)}$ due to its longer decay length of ~ 67 μm . And since the modulating envelope with K_{beat} requires the presence of both components at the air/silver interface, the decay length of the envelope is dictated by the component having the shortest of the two decay lengths, which in this example is 3.2 μm associated with the $C_{\delta_g} e^{i(k_g x - \omega t)}$. Experimental measurements of such effects, however, may not be possible. Although measurements carried out by Verhagen *et. al.* [2] may be valid, Wang *et. al.*[1] correctly pointed out that positioning any probe such as an AFM tip, in the vicinity of the slit establishes standing wave oscillations between the tip and the slit, leading to a series of minima/maxima that convolve with those of the interference envelope. FEM simulations has confirmed this.

192

2.2 Plasmonic Time Crystal

193

194

195

196

197

198

199

200

With diamond (or glass) substrate, when the film thickness is that of the skin depth, SPPs are no longer confined to the surface of the metal but rather penetrate the film from the substrate and superstrate and interfere with one another inside the film. However, (as it is the case here), due to the aperture dimensions and partially due to the $\epsilon_m E_{zm} = \epsilon_d E_{zd}$ [8], normal to the surface component of the electric field at the diamond/silver boundary is much stronger than those at the air/silver at $\lambda_0 = 700$ nm, hence $E_{zg} \gg E_{za}$. Therefore, fields from the substrate dominate the film. Furthermore, the x -component of the SPP was found to be stronger than its z -components at $\lambda_0 = 700$ nm, i.e.

201

$$E_{xg} \approx 2E_{zg} \text{ calculated using } E_{xg} = -i\sqrt{\frac{-\epsilon_m}{\epsilon_d}} E_{zg} \text{ [8], and in agreement with the numerical results.}$$

202

203

204

Consequently a trail of z -component of the electric field $\{\dots 0 - 0 + 0 - 0 \dots\}$ carries a trail of x -component $\{\dots - 0 + 0 - 0 + \dots\}$ with "+", "0" and "-" denoting $+E_{xz}$, 0 and $-E_{xz}$ respectively. Note the 90° phase difference between the x and the z -components. Naturally, the induced periodic polarization, travels inside the film as the SPPs propagate over the surface. The x -component of the

205 polarization, $P_{xg} = \epsilon_0 \chi_e E_{xg} e^{i(k_g x - \omega_0 t)}$, is of interest in the context of plasmonic time crystals as it
 206 signifies periodic accumulation of conduction electrons along the x -axis, hence periodic
 207 screening/transparency within the film. With a flat metallic film that extends to infinity in the
 208 x -direction, it is not possible to apply the Gauss's law to calculate the charges due to SPP fields.
 209 Therefore, I have provided an alternative approach to calculate the induced periodic charge density
 210 due to propagating E_{zg} :

$$211 \quad \Delta \rho_x = -\frac{\omega_0}{c} \epsilon_0 \epsilon_m^* \left[\frac{\epsilon_d + \epsilon_m}{\sqrt{\epsilon_m + \epsilon_d}} \right] E_{zg} e^{i(k_g x - \omega_0 t)} \quad (5)$$

212 see Appendix B. And in terms of number of electrons being displaced:

$$213 \quad \Delta N = \frac{\Delta \rho_x}{e^-} = -\frac{\omega_0}{c e^-} \epsilon_0 \epsilon_m^* \left[\frac{\epsilon_m + \epsilon_d}{\sqrt{\epsilon_m + \epsilon_d}} \right] E_{zg} e^{i(k_g x - \omega_0 t)} \quad (6)$$

214 Equation (6) reveals the total number of charges being displaced per SPP field. Given that the
 215 fermi energy level for metals is given by [15]:

$$216 \quad \mathcal{E}_F = \frac{h^2}{8m} \left(\frac{3N}{\pi} \right)^{2/3} \quad (7)$$

217 one must set $N = N_0 + \Delta N$, where N_0 is the number of electrons per unit volume when unperturbed.
 218

219 Consequently, \mathcal{E}_F becomes a function $E_{zg} e^{i(k_g x - \omega_0 t)}$, which may lead to many interesting effects, such as
 220 periodic refractive index, fermi levels, local work functions, density of states, eigen energies inside
 221 film, which will be a topic of another report. Nevertheless, in the absence of any incident field over
 222 the film, for example when the SPPs are launched by a dipole near the surface [16], the propagation
 223 of surface waves, and all physical quantities they carry, is unperturbed. However, in the presence of
 224 an incident field from the substrate, the superposition of the field inside the film is given by
 225 $E = E_{xi} e^{i(k_x z - \omega_0 t)} + E_{xg} e^{i(k_g x - \omega_0 t)}$ which create disturbance on the periodic charges densities. It is intuitive
 226 that loci polarized by $+E_{xg}$ be transparent to $+E_{xi}$, and vice versa. Now, consider an arbitrary time
 227 $t = t_0$, when the maximum of the incident electric field falls over the film. This is depicted by the
 228 following notation:

$$229 \quad \frac{E_{xg}(x, t_0): +, 0, -, 0, +}{E_{xi}(t_0): +, +, +, +, +} \Rightarrow +, +, 0, +, + \quad (8)$$

230 This scenario is shown in Figure 4 with the periodic arrangement of "0"s when the maximum of
 231 the field falls over the film. Also note the strong periodic field under the film, inside the substrate! At
 232 $t = t_0 + T/2$, hence 180° phase, both E_{xg} and E_i change signs. This will lead to:

$$233 \quad \frac{E_{xg}(x, t_0 + T/2): -, 0, +, 0, -}{E_{xi}(t_0 + T/2): -, -, -, -, -} \Rightarrow -, -, 0, -, - \quad (9)$$

234 with "0" remained intact in space. This scenario is also confirmed by numerical results.

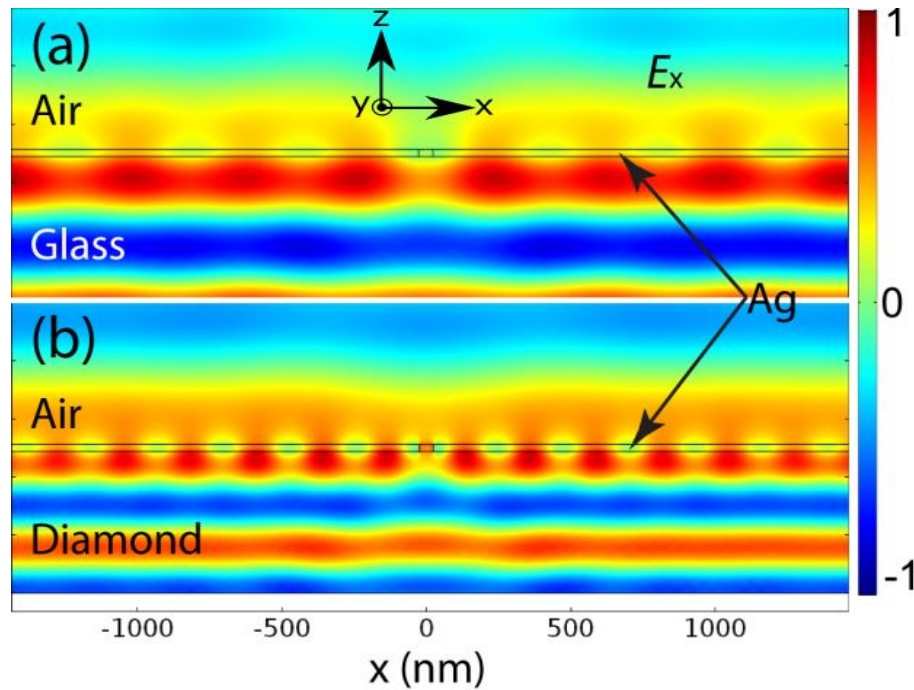
235

236 *It is intuitive to think of the periodic "0"s as loci where conduction electrons are trapped. If this hypothesis*
 237 *is validated by experiment, it would open doors to study new phenomena. Each "0" may be viewed as a*
 238 *super-atom with oversaturated electronic orbitals, elevated fermi level, lowered work function and many more*
 239 *effects when considered in periodic settings which I have highlighted in the conclusion.*

240

241 Back to causality, at the first glance it seems it is a simple matter of superposition of two
 242 orthogonally propagating EM waves with the x -component of the two fields summed up inside the
 243 film. However, a close look at the numerical results revealed that when E_{xi} drops to 0, (e.g. at

244 $t = t_0 + T/4$), polarization inside the film experiences the effect of $E_{xi}(t_0)$. This 90° phase difference
 245 between applied field and the reaction is attributed to the charge bundles experiencing the Lorentz
 246 force $F_{xg} = J_{zg} (B_{yg} + B_{yi})$. Furthermore, since B_{yi} is 0 at $t = t_0 + T/4$, the restoration of periodic potential
 247 is resumed at $t = t_0 + T/4$ but completed at $t = t_0 + T/2$ when $-E_{xi}$ falls over the film. The whole
 248 creation/anhelation of $P_x = \epsilon_0 \chi_e E_x$ is a sinusoidal process in time. Numerical results also revealed
 249 that E_{zg} not being affected by the *incident* field. Therefore, the restoration process is attributed to the
 250 E_{zg} .



251

252 Figure 4: Snapshot of electric field E_x passing through a periodic charge screen (with periodicity $1/K_g$)
 253 formed inside the 25 nm thick silver film for (a) glass and (b) diamond substrates. Note that E_x was
 254 calculated at an arbitrary time with the maximum of its amplitude falling over the silver film.

255 Since this creation/anhelation is periodic both in time and space with periodicities $T/2$ and λ_g ,
 256 hence oscillating at frequency other than that of the drive, (although not an expert in the topic), I
 257 believe it qualifies as a time crystal [17,18]. As for the breaking time symmetry, I need access to
 258 certain resources only academics enjoy, but as an alumnus, this is not possible at this stage.
 259 However, I must remind the readers that the x -component of the SPP's electric field (as I
 260 understand) must always lag its z -components by 90° at *resonance*, a condition satisfied for SPPs
 261 launched by an aperture at any frequency. The term *crystal* also implies that one should be able to
 262 define both the Hamiltonian to determine the eigen-energies and the Schrödinger equation to
 263 explain the De Broglie's matter waves [19,20] for that system. Could it be called a *crystal* otherwise?
 264 The potentials V , experienced by electrons in a time crystal and consequently, wave functions ψ and
 265 eigen-energies ξ , must naturally be time-dependent:

$$266 \quad \xi_j(t)\psi_j(\mathbf{R}_j, t) = \hat{H}(t)\psi_j(\mathbf{R}_j, t) \quad (10)$$

$$267 \quad ih \frac{\partial \psi_j(\mathbf{R}_j, t)}{\partial t} = \hat{H}(t)\psi_j(\mathbf{R}_j, t) \quad (11)$$

268

269 Considering the original Hamiltonian, \hat{H} , for the many-electrons [21]:

270

$$271 \quad \hat{H} = \sum_j \left[-\frac{\hbar^2}{2m} \nabla_j^2 + V(\mathbf{R}_j) \right] + \frac{1}{2} \sum_{\substack{j,k \\ j \neq k}} \frac{e^2}{4\pi\epsilon |\mathbf{R}_j - \mathbf{R}_k|} \quad (12)$$

272 time variations of kinetic energy term in equation (12) is taken care of by the time-dependent wave
 273 function $\psi_j(\mathbf{R}_j, t)$, however, one must introduce the notion of time into equation (12) and rewrite it
 274 as:

$$275 \quad \hat{H}(t) = \sum_j \left[-\frac{\hbar^2}{2m} \nabla_j^2 + V(\mathbf{R}_j(t)) \right] + \frac{1}{2} \sum_{\substack{j,k \\ j \neq k}} \frac{e^2}{4\pi\epsilon |\mathbf{R}_j(t) - \mathbf{R}_k(t)|} \quad (13)$$

276 where $V(\mathbf{R}_j(t)) = V_{ext}(\mathbf{R}_j(t)) + V_i(\mathbf{R}_j(t), t)$, V_{ext} is the potential due to the positive ions, $V_i \propto e^{i(k_s x - \omega t)}$ is
 277 the time-dependent potential due to the creation/annihilation of charge bundles and \mathbf{R}_j is the position
 278 vector of the j^{th} electron. Note that by making $\mathbf{R}_{j,k}$ time-dependent, $j \neq k$ is taken care of, however, V_i
 279 has both time and spatial dependence (other than that of positive ions). Time-dependent
 280 Hamiltonian in Equation (13) implies that the computation must trace the position of each electron,
 281 \mathbf{R}_j with respect to t and the changes in potential with respect to t and \mathbf{R}_j . The Hartree
 282 approximations [21] are also based on time-independent electron-electron interactions, so it must be
 283 remedied accordingly for time crystals. An interesting article by Linde [22] may prove to be useful to
 284 investigate possible changes to the effective mass and conductivity in an applied field but that also
 285 needs to be modified. With the advent of High Performance Computing (HPC) ab initio modelling
 286 and simulations of matters where the constituting components are atoms and electrons are
 287 becoming more accessible. An article by Borysov *et al.* [23] provides a background on the existing
 288 infrastructure for numerically modelling and investigating structures at atomic levels using the
 289 Density Functional Theory (DFT) calculations, which may prove to be a platform of choice to study
 290 time crystals.
 291

292 5. Conclusions, and Roadmaps for Further Study

293 In conclusion, it was shown that for a sufficiently thin silver film sandwiched between two
 294 different dielectrics, the mixing of the two SPPs (formed at the substrate and the superstrate)
 295 produce an interference envelope that modulates the travelling SPPs at the substrate. For film
 296 thicknesses equivalent to the SPP's penetration depth, surface waves from optically denser
 297 dielectric/metal interface would dominate, leading to volume plasmons that propagate inside the
 298 film at optical frequencies. Interference of such volume with the incident field over the film creates
 299 charge bundles that are periodic in space and time. Although many questions remained unanswered
 300 in this report, the future work will focus on them. If I can hypothesize, the presence of charge
 301 bundles inside the film may imply changes to the electronic density of states, electron-electron
 302 collision (hence the mean free path), electron-lattice interaction (hence the electron's effective mass)
 303 and consequently conductivity, due to the presence of an additional periodic potential that may
 304 compete or superpose with that of the positive ions. It is intuitive to think of the periodic "0"s as loci
 305 where electrons trapped. If this hypothesis is validated by experiment, it would open doors to study
 306 new phenomena. Each "0" may be viewed as super-atom with oversaturated electronic orbitals,
 307 elevated fermi level, lowered work function and many more effects when considered in periodic
 308 settings which are analogous to that of a superlattice in semiconductors[21].

309 **Conflicts of Interest:** The author declares no conflict of interest. There were no founding sponsors behind this
 310 work. Apart from the named author, no other entity had any role in the design of the study; in the collection,
 311 analyses, or interpretation of data; in the writing of the manuscript, and in the decision to publish the results".

312 Appendix A - Superposition

313 To explain the overlap between the beat modulation and the second harmonics in the envelope
 314 when $n_1 = 2.41$ at $\lambda_0 = 700$ nm, consider the superposition of two waves having equal amplitudes
 315 propagating along the x -axis i.e. $\Psi(x, t) = e^{i(k_1x - \omega_1t)} + e^{i(k_2x - \omega_2t)}$, which can be written as:

$$316 \quad \Psi(x, t) = 2e^{i\left(\frac{(k_1+k_2)x}{2} - \frac{(\omega_1+\omega_2)t}{2}\right)} \cos\left(\frac{(k_1-k_2)x}{2}\right) \cos\left(\frac{(\omega_1-\omega_2)t}{2}\right) \quad (14)$$

317 Here it is assumed both waves start in phase. This form of the equation is of interest since it
 318 separates the terms related to the coherent length, $4\pi/(k_1+k_2)$, and the coherent time,
 319 $4\pi/(\omega_1+\omega_2)$ of the superposed travelling wave. Furthermore, the last two cosine terms indicate that
 320 the combined travelling wave is modulated by two envelopes having nodes (or anti-nodes)
 321 separated by $\left|\cos\left(\frac{(k_1-k_2)x}{2}\right)\right|$ in space and $\left|\cos\left(\frac{(\omega_1-\omega_2)t}{2}\right)\right|$ in time. In other words the beat
 322 frequencies in space and time are $|k_1-k_2|$ and $|\omega_1-\omega_2|$ respectively, therefore the coherent lengths
 323 (for a lack of a better word) of the envelopes in space and time can be calculated as $2\pi/(k_1-k_2)$
 324 and $2\pi/(\omega_1-\omega_2)$ respectively. Necessary conditions to eliminate undesirable jitters in space and
 325 time envelopes are:

$$326 \quad [2\pi/(k_1-k_2)] = [4\pi/(k_1+k_2)] \quad (15)$$

327 AND

$$328 \quad [2\pi/(\omega_1-\omega_2)] = [4\pi/(\omega_1+\omega_2)] \quad (16)$$

329 In the case of two superposed SPP waves at the air/silver interface, the superposition may be
 330 simplified to:

$$331 \quad \sigma(x, t) = e^{-i\omega_0t} \left[C_a e^{i(k_a x)} + C_{\delta_g} e^{i(k_g x)} \right] \quad (17)$$

332 Furthermore, in the case of 25 nm silver film $C_{\delta_g} \approx C_a$, see Figure 2(c) and (e). Under such
 333 conditions, equation (17) may be written for the spatial terms as:

$$334 \quad \sigma(x) = \left[2e^{i\left(\frac{(k_a+k_g)x}{2}\right)} \cos\left(\frac{(k_a-k_g)x}{2}\right) \right] \quad (18)$$

335 Equation(18), which is the special case of equation(14), shows the coherent length of the
 336 combined travelling SPP waves to be $4\pi/(k_a+k_g)$ with the beat modulation occurring according to
 337 $2\pi/|k_a-k_g|$. A necessary condition to overlap the coherent length and the beat modulation with the
 338 second harmonics in the envelope is then:

$$339 \quad 1/2k_a = 2\pi/|(k_a-k_g)| = 4\pi/(k_a+k_g) \quad (19)$$

340 In this report, numerical values for wavenumbers obtained from FFT
 341 showed $1/2K_a \approx 1/|K_a-K_g| \approx 2/|K_a+K_g|$ at $\lambda_0 = 700$ nm when $n_1 = 2.41$. Clearly in the case of a glass
 342 substrate with $n_1 = 1.52$, $1/2K_a \neq 1/|K_a-K_g| \neq 2/|K_a+K_g|$ at $\lambda_0 = 700$ nm.

343 The appendix is an optional section that can contain details and data supplemental to the main
 344 text. For example, explanations of experimental details that would disrupt the flow of the main text,
 345 but nonetheless remain crucial to understanding and reproducing the research shown; figures of
 346 replicates for experiments of which representative data is shown in the main text can be added here
 347 if brief, or as Supplementary data. Mathematical proofs of results not central to the paper can be
 348 added as an appendix.

349 Appendix B - Lorentz Force and Induce Charges Inside the Film

350 Let the magnetic flux density and the electric field carried by SPPs be denoted by:

351

$$352 \quad \mathbf{B}_m = (0, B_y, 0) e^{i(k_x x + k_z z - \omega_0 t)}$$

$$353 \quad \mathbf{E}_m = (E_x, 0, E_z) e^{i(k_x x + k_z z - \omega_0 t)}$$

354 For simplicity, ignoring the exponent terms, we are interested in $F_x = J_z B_y$, where $J_z = \sigma_e E_z$.

$$355 \quad \text{Given that } \mathbf{B}_m = \frac{\nabla \times \mathbf{E}_m}{j\omega_0}$$

356 and

$$357 \quad \nabla \times \mathbf{E}_m = \begin{pmatrix} \partial_x \\ \partial_y \\ \partial_z \end{pmatrix} \times \begin{pmatrix} E_x \\ 0 \\ E_z \end{pmatrix} = \begin{pmatrix} \partial_y E_z \\ -\partial_x E_z + \partial_z E_x \\ \partial_y E_x \end{pmatrix} \quad (20)$$

358 In 2D:

$$359 \quad \nabla \times \mathbf{E}_m = \begin{pmatrix} 0 \\ -ik_x E_z + ik_z E_x \\ 0 \end{pmatrix} \quad (21)$$

360 One can write $B_y = \frac{k_x E_z - k_z E_x}{\omega_0}$. The Lorentz force distribution along the x-axis is then

$$361 \quad F_x = J_z B_y = \sigma_m E_z \frac{k_x E_z - k_z E_x}{\omega_0}. \text{ This can be further reduced by } E_x = -i\sqrt{\frac{-\epsilon_m}{\epsilon_d}} E_z \text{ to:}$$

$$362 \quad F_x = \frac{\sigma_m}{\omega_0} \left[k_x + k_z \left(i\sqrt{\frac{-\epsilon_m}{\epsilon_d}} \right) \right] E_z^2 \quad (22)$$

363 Using equations (1)-(2) and replacing $\sigma_m = \omega_0 \epsilon_0 \epsilon_m^*$ [24], the Lorentz force becomes:

$$364 \quad F_x = \frac{\omega_0 \epsilon_0 \epsilon_m^*}{c} \left[\frac{\sqrt{\epsilon_m \epsilon_d} + i\epsilon_m \sqrt{\frac{-\epsilon_m}{\epsilon_d}}}{\sqrt{\epsilon_m + \epsilon_d}} \right] E_z^2 \quad (23)$$

365

366 The volume charge profile along the x-direction due to only the Lorentz force may be calculated

367 as $\Delta\rho_x = F_x / E_x$ where $E_x = -i\sqrt{\frac{-\epsilon_m}{\epsilon_d}} E_z$, therefore:

$$368 \quad \Delta\rho_x = -\frac{\omega_0}{c} \epsilon_0 \epsilon_m^* \left[\frac{\epsilon_d + \epsilon_m}{\sqrt{\epsilon_m + \epsilon_d}} \right] E_z \quad (24)$$

369 And in terms of number of free electrons:

$$370 \quad \Delta N = \frac{\Delta\rho_x}{e^-} = -\frac{\omega_0}{ce^-} \epsilon_0 \epsilon_m^* \left[\frac{\epsilon_d + \epsilon_m}{\sqrt{\epsilon_m + \epsilon_d}} \right] E_z \quad (25)$$

371

372 **References**

- 373 1. Wang, L.M.; Zhang, L.X.; Seideman, T.; Petek, H. Dynamics of coupled plasmon polariton wave packets
374 excited at a subwavelength slit in optically thin metal films. *Phys. Rev. B* **2012**, *86*.
- 375 2. Verhagen, E.; Dionne, J.A.; Kuipers, L.; Atwater, H.A.; Polman, A. Near-field visualization of strongly
376 confined surface plasmon polaritons in metal-insulator-metal waveguides. *Nano Lett.* **2008**, *8*, 2925-2929.
- 377 3. Davis, T.J. Surface plasmon modes in multi-layer thin-films. *Opt. Commun.* **2009**, *282*, 135-140.
- 378 4. Berini, P. Long-range surface plasmon polaritons. *Advances in Optics and Photonics* **2009**, *1*, 484-588.
- 379 5. Ortuno, R.; Garcia-Meca, C.; Rodriguez-Fortuno, F.J.; Marti, J.; Martinez, A. Role of surface plasmon
380 polaritons on optical transmission through double layer metallic hole arrays. *Phys. Rev. B* **2009**, *79*.
- 381 6. Djalalian-Assl, A. Optical nano-antennas. PhD, The University of Melbourne, Melbourne, 2015.
- 382 7. Novotny, L.; Hecht, B. *Principles of nano-optics*. Cambridge, U.K. : Cambridge University Press, 2006.: 2006.
- 383 8. Rosa, A.L. Lectures 9: Surface plasmon polaritons.
384 http://web.pdx.edu/~larosaa/Applied_Optics_464-564/Lecture_Notes_Posted/2010_Lecture-7_SURFACE%20PLASMON%20POLARITONS%20AT%20%20METALINSULATOR%20INTERFACES/Lecture_on_the_Web_SURFACE-PLASMONS-POLARITONS.pdf
- 385
- 386
- 387 9. Palik, E.D. *Handbook of optical constants of solids*. Academic Press: San Diego, 1985; p 350.
- 388 10. Dai, W.; Soukoulis, C.M. Theoretical analysis of the surface wave along a metal-dielectric interface. *Phys.*
389 *Rev. B* **2009**, *80*, 155407.
- 390 11. Nikitin, A.Y.; Garcia-Vidal, F.J.; Martin-Moreno, L. Surface electromagnetic field radiated by a
391 subwavelength hole in a metal film. *Phys. Rev. Lett.* **2010**, *105*.
- 392 12. Main, I.G. *Vibrations and waves in physics*. Cambridge University Press: 1987.
- 393 13. Phillip, H.R.; Taft, E.A. Kramers-kronig analysis of reflectance data for diamond. *Physical Review a-General*
394 *Physics* **1964**, *136*, 1445-&.
- 395 14. Fairchild, B.A.; Olivero, P.; Rubanov, S.; Greentree, A.D.; Waldermann, F.; Taylor, R.A.; Walmsley, I.;
396 Smith, J.M.; Huntington, S.; Gibson, B.C., *et al.* Fabrication of ultrathin single-crystal diamond membranes. *Adv.*
397 *Mater.* **2008**, *20*, 4793-4798.
- 398 15. Eisberg, R.M.; Resnick, R. *Quantum physics of atoms, molecules, solids, nuclei, and particles*. 2nd ed.; Wiley:
399 New York, 1985.
- 400 16. Djalalian-Assl, A. Dipole emission to surface plasmon-coupled enhanced transmission in diamond
401 substrates with nitrogen vacancy center- near the surface. *Photonics* **2017**, *4*, 10.
- 402 17. Wilczek, F. Quantum time crystals. *Phys. Rev. Lett.* **2012**, *109*, 5.
- 403 18. Shapere, A.; Wilczek, F. Classical time crystals. *Phys. Rev. Lett.* **2012**, *109*, 4.
- 404 19. Ashcroft, N.W.; Mermin, N.D. *Solid state physics*. Holt: New York,, 1976; p xxi, 826 p.
- 405 20. Blümel, R. *Advanced quantum mechanics the classical-quantum connection*. Jones and Bartlett Publishers:
406 Sudbury, Mass., 2011; p xii, 425 p.
- 407 21. Davies, J.H. *The physics of low-dimensional semiconductors : An introduction*. Cambridge University Press:
408 Cambridge, U.K. ; New York, NY, USA, 1998; p xviii, 438 p.
- 409 22. Linde, J.O. The effective mass of the conduction electrons in metals and the theory of superconductivity.
410 *Physics Letters* **1964**, *11*, 199-201.
- 411 23. Borysov, S.S.; Geilhufe, R.M.; Balatsky, A.V. Organic materials database: An open-access online database
412 for data mining. *Plos One* **2017**, *12*, 14.
- 413 24. Lorrain, P.; Corson, D.R.; Lorrain, F. *Electromagnetic fields and waves : Including electric circuits*. Freeman:
414 New York, 1988.